Investigation on Interaction of Explosively Formed Projectile with Multi-layer Medium Targets

C Wang[1]*, W Xu[1], Y Bi[2]

1. State Key Laboratory of Explosion Science and Technology, Beijing Institute of Technology, China
2. College of Science, North University of China, China

ABSTRACT

To investigate the influence of liner material, charge diameter and standoff on explosively formed projectile (EFP) penetrating into multi-layer targets, a large number of experiments were performed and the experimental data on crater diameter, hole diameter, crater depth and penetration depth were obtained. Meanwhile, the numerical simulation have been done to study the formation and penetration processes of all the EFP with AUTODYN software. The numerical results of penetration depth are in good agreement with the experimental ones. The results indicate that the optimal liner material of EFP to achieve a larger penetration hole diameter and depth are aluminum and copper, respectively.

1. INTRODUCTION

The impact resistance of concrete structures is of major importance in engineering application. In recent years, a large number of scholars investigated the intrinsic mechanisms on penetrating into concrete [1-3]. Nia et al. [4] studied the resistance of concrete target against penetration of eroding long rod projectile. The analysis results show that there is a proportional relation between the strength of the target and the size of the incompressible zone. Smith et al. [5] developed a discrete modeling of ultra-high-performance concrete named CORTUF which can be used to simulate the behavior of protective CORTUF panels subjected to projectile penetration. In order to investigate the intrinsic mechanisms of mass loss for a projectile penetration into concrete, Guo et al. [6] carried out experiments on 30CrMnSiNi2A kinetic energy projectiles with an ogival nose penetrating concrete targets in the normal direction at a striking velocity of 843 m/s and 1400 m/s, respectively. Based on the experimental analysis and observations by using an optical microscope, energy dispersive X-ray detector and microhardness tester, evolution mechanisms of the microstructures induced by plastic deformation and high temperature during penetration were proposed. Warren et al. [7] designed experiments to recon deceleration date from projectile penetration into concrete targets with compressive strengths of 23MPa and 39MPa and two empirical penetration models that described deceleration kinetic energy divided by projectile mass were developed. A meshfree formulation under the reproducing kernel particle method was introduced by Sherburn et al. [8] for modeling the penetration and perforation of concrete slab. The accuracy

*Corresponding Author: wangcheng@bit.edu.cn

of the formulation was confirmed by simulation. Wang et al. [9] investigated shaped charge penetrating into concrete targets experimentally, numerically and theoretically. Bian et al. [10] developed an elastoplastic damage model for concrete with an emphasis on the pressure dependence of volume change. The numerical results of penetrating into concrete targets by using the proposed model are in good agreement with the experimental results. Experimental and numerical investigations are conducted by Feng et al. [11] to study the dynamic response of a double-layered target of ultra-high-performance fibre reinforced concrete and armour steel subjected to an armour-piercing projectile impact. Yu et al. [12] investigated the energy absorption capacity of a sustainable Ultra-High Performance Fibre Reinforced Concrete (UHPFRC) under high velocity projectile impact. The experimental results indicate that, under high velocity projectile impact, the UHPFRC mixture with hybrid fibres shows a much better energy absorption capacity than the one with hooked steel fibres only, particularly in resisting the scabbing at the rear surface.

The penetrating into multi-layer targets is a complex mechanical problem which usually involves shock wave propagation, dynamic behavior of multi-layer targets, interactions between different layers and so on. Investigations on penetrating into multi-layer targets are far less than that of pure concrete targets. Zeng et al. [13] simulated the progress of penetrating obliquely multi-layer runway with anti-runway penetrator by the finite element code LS-DYNA 3D. The result indicated that the overturned angle of projectile could be reduced and the penetration depth increases when the centroid of projectile was moved ahead. The damage effects of the multi-layered target against reactive materials based shaped charge was studied in reference [14].

In the present investigations, due to lack of systematic experimental data, the intrinsic mechanisms of EFP penetrating into multi-layer targets are not understood clearly. We carried out a series of experiments of penetrating into multi-layer targets by EFP. Using both experiments and numerical simulations, we investigated the variation laws of crater diameter, hole diameter, crater depth and penetration depth with different liner materials, charge diameters and standoffs.

2. EXPERIMENTAL SCHEME

The charge with diameters of 100mm and 120mm are designed and Composition B with density of 1.6g/cm^3 is selected as the main charge in experiments. As shown in Figure 1, the length to diameter ratio of these shaped charge is 1:1. The cone angle of the liner is 120° and its wall thickness is uniformly 0.03D, for which liner materials include steel, copper and aluminum. Five kinds of standoffs (L=1D, 1.5D, 2D, 3D and 4D) are investigated respectively in this paper, which D is defined as charge diameter here.

The multi-layer targets consist of three layers in the experiments, as shown in Figure 2. The surface layer is concrete. Its density is 2.4g/cm^3, compressive strength 30MPa and thickness 400mm. The middle layer is pebble. Its thickness is 300mm. The bottom layer is rammed earth. Its thickness is 400mm.

The typical experimental setup and result are shown in Figures 3. The values of crater diameter D_1, hole diameter D_2, crater depth H_1 and penetration depth H are measured in the experiments as shown in Figure 4. The maximum and minimum values of D_1 and D_2 are recorded, and then the averages of maximum and minimum values are adopted to depict variation curves, as shown in Figures 5 and 6.

Figure 1: Shaped charge structure in experiments

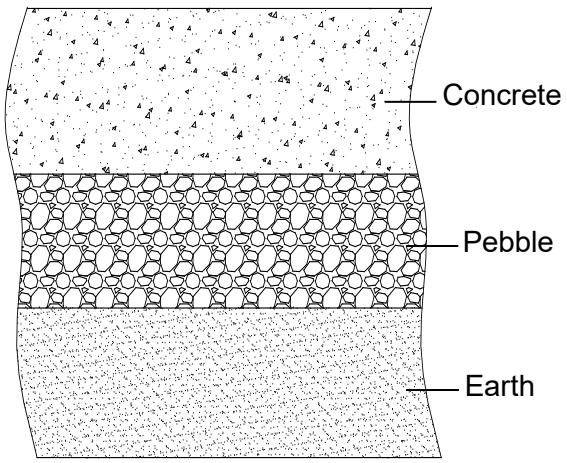

Figure 2: Schematic of multi-layer targets.

(a) (b)

Figure 3: (a) The typical experimental setup. (b) The typical experimental result

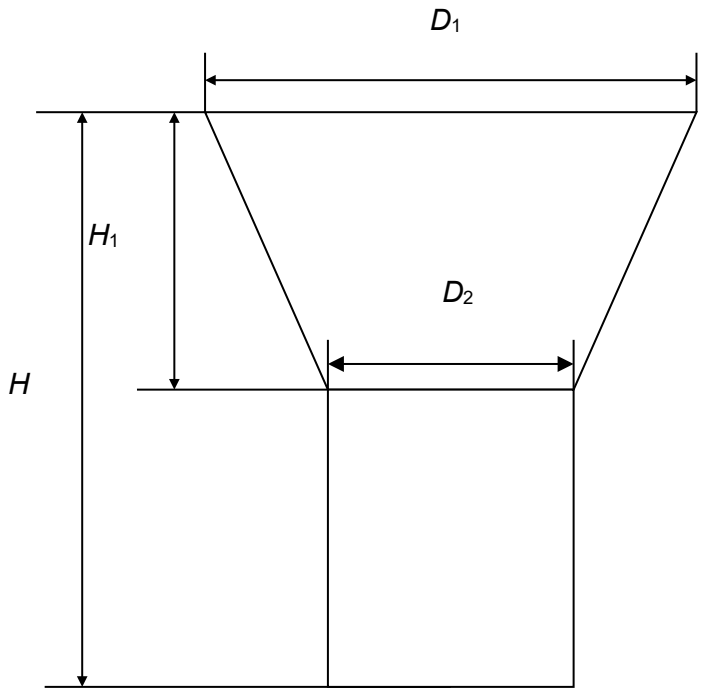

Figure 4: Schematic of multi-layer targets

3. EXPERIMENTAL RESULTS

3.1. Results of Crater Diameter D_1

For different charge diameters, with the increase of standoffs, the variation trend of crater diameter which caused by EFP with steel liner or copper liner are nearly the same, as shown in Figure 5. Crater diameters formed by EFP with steel liner increase firstly and then decrease with the increase of standoffs; Table 1 illustrate that, when the charge diameters are 100mm and 120mm respectively, the corresponding maximum values of crater diameters are 7.6D and 7.5D; for the same standoff, crater diameter formed by EFP with 120mm diameters are larger than that formed by EFP with 100mm. Crater diameters formed by EFP with copper liner decrease firstly and then increase with the increase of standoffs; when the charge diameters are 100mm and 120mm respectively, the corresponding maximum values of crater diameters are 5.5D and 6.7D. Except for 1.5D standoff, crater diameters caused by EFP with aluminium liner vary slightly with the increase of standoffs; when charge diameters are 100mm and 120mm respectively, the corresponding maximum values of crater diameters are 6.2D and 6.3D; for the same standoff, crater diameter formed by EFP with 120mm diameters are larger than that formed by EFP with 100mm. When standoffs are lower than 2D, crater diameters caused by EFP with steel liner, aluminium liner and copper liner decrease in sequence. In the case of standoffs are greater than 2D, crater diameters caused by EFP of steel liner decrease rapidly with the increase of standoffs and crater diameters caused by EFP with aluminium liner are the largest.

Table 1: Experimental results of crater diameter with different liner materials, charge diameters under different standoffs (mm)

Liner material	Diameter (mm)	Standoff				
		1D	1.5D	2D	3D	4D
Steel	100	570×590	720×800	600×600	420×450	370×400
	120	810×810	880×930	580×700	510×550	400×510
Copper	100	500×550	290×300	280×280	350×370	440×440
	120	710×730	520×520	470×530	300×320	400×400
Aluminum	100	500×570	600×630	500×530	500×500	470×510
	120	750×750	620×620	700×710	640×750	700×750

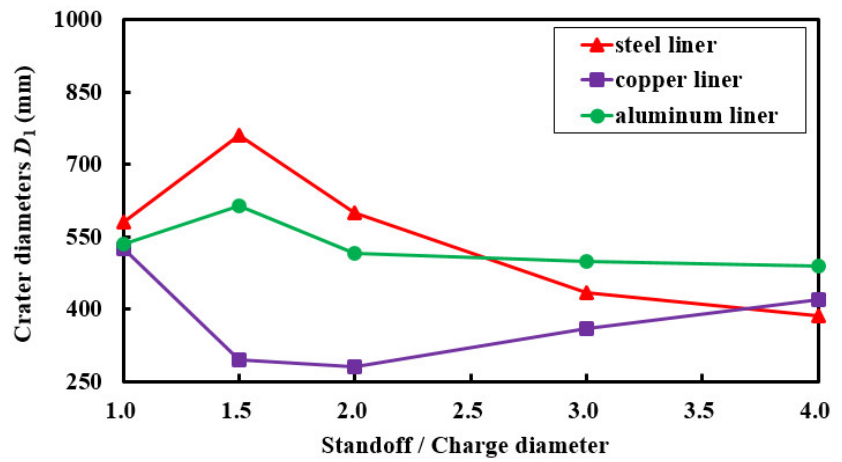

(a)

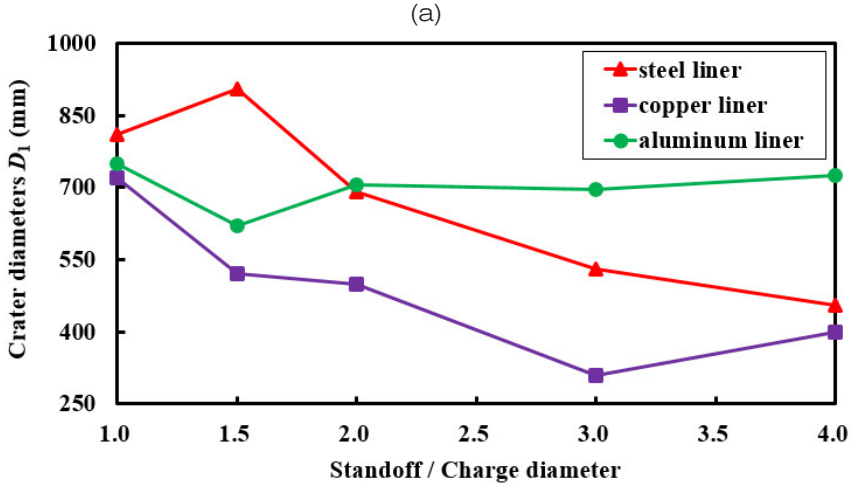

(b)

Figure 5: Variation trend of D1 with different standoffs (a) D=100mm. (b) D=120mm

3.2. Results of Hole Diameter D_2

It is obvious from Figure 6 that, for different charge diameters, with the increase of standoffs, the variation trend of hole diameter which caused by EFP with steel liner or copper liner are nearly the same. Hole diameters formed by EFP with steel liner increase firstly and then decrease with the increase of standoffs; when the charge diameters are 100mm and 120mm respectively, the corresponding maximum values of hole diameters are 1D and 0.9D, as set out in Table 2. Hole diameters caused by EFP with copper liner decrease with the increase of standoffs; the maximum value of hole diameter is 0.6D for both 100mm and 120mm charge diameters. Among different liner materials, hole diameters caused by EFP with copper liner are the smallest. There are no stable variation laws of hole diameter which caused by EFP with aluminium liner; when the charge diameters are 100mm and 120mm respectively, the corresponding maximum values of hole diameters are 1.3D and 1.7D. For different liner materials and constant charge diameters, hole diameters caused by EFP with aluminium liner are the largest. It indicates that the EFP with aluminium liner is suitable for penetrating larger hole diameters.

Table 2: Experimental results of hole diameter with different liner materials, charge diameters under different standoffs (mm)

Liner material	**Diameter (mm)**	**Standoff**				
		1D	**1.5D**	**2D**	**3D**	**4D**
Steel	100	85×85	100×100	60×60	37×47	30×45
	120	90×100	100×120	60×60	50×56	40×50
Copper	100	60×60	35×35	32×32	30×30	27×27
	120	70×70	40×40	40×40	30×40	35×35
Aluminum	100	100×100	110×110	130×130	100×100	75×75
	120	120×120	155×155	90×90	200×200	50×50

3.3. Results of Crater Depth H_1

From Table 3 we can find that crater depths caused by EFP with steel liner decrease with the increase of standoffs; when the charge diameters are 100mm and 120mm respectively, the corresponding maximum values of crater depths are 1.7D and 1.6D; for the same standoff,

Table 3: Experimental results of crater depth with different liner materials, charge diameters under different standoffs (mm)

Liner material	**Diameter (mm)**	**Standoff**				
		1D	**1.5D**	**2D**	**3D**	**4D**
Steel	100	165	160	143	130	115
	120	189	180	150	142	115
Copper	100	125	75	95	98	110
	120	164	130	115	122	100
Aluminum	100	140	135	142	155	147
	120	165	155	170	145	180

crater depth formed by EFP with 120mm diameter is larger than 100mm charge's. When the charge diameters are 100mm and 120mm respectively, the corresponding maximum values of crater depths caused by EFP with copper liner are 1.3D and 1.4D. For 100mm and 120mm charge diameters respectively, the maximum values of crater depths caused by EFP with aluminium liner are 1.6D and 1.5D. As shown in Figure 7, crater depths formed by EFP with steel liner are the largest under condition of standoffs lower than 2D. When standoffs greater than 2D, crater depths caused by EFP with aluminium liner are the largest. Among different liner materials, crater depths caused by EFP with copper liner are the smallest.

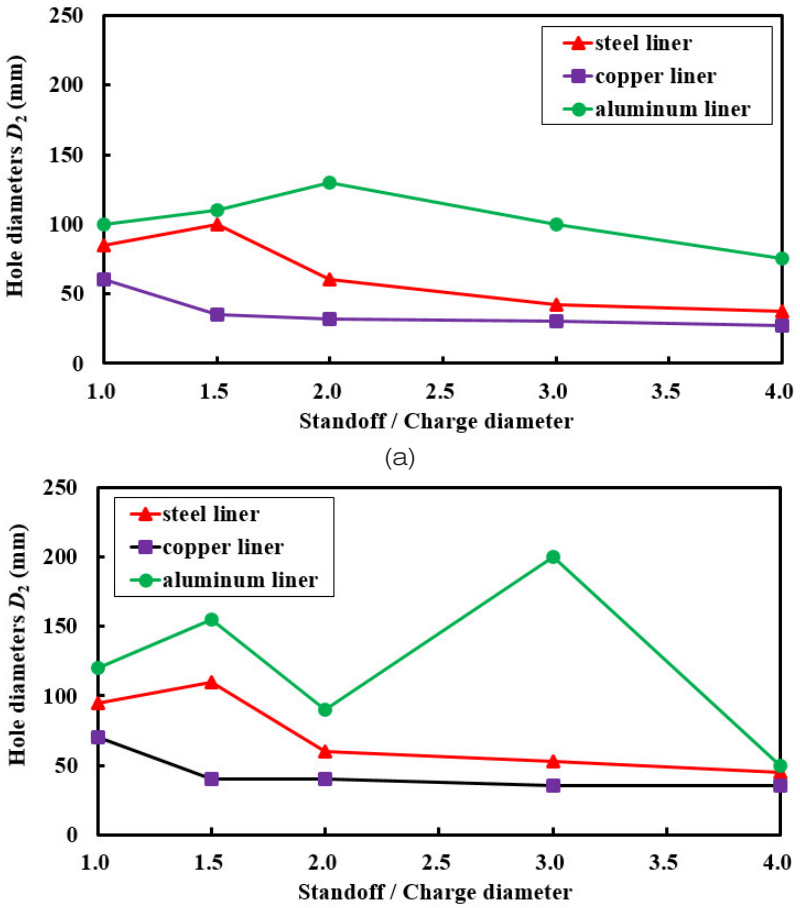

Figure 6: Variation trend of D_2 with different standoffs (a) D=100mm. (b) D=120mm

3.4. Results of Penetration Depth H

It is clear from Figure 8 that penetration depths caused by EFP with steel liner increase with the increase of standoffs; as shown in Table 4, when the charge diameters are 100mm and 120mm respectively, the corresponding maximum values of penetration depths are 5.6D and 5.8D. In the case of 100mm charge diameters, the maximum value of penetration depths

caused by EFP with copper liner is 9.5D. In the case of 120mm charge diameters and 4D standoff, EFP with copper liner through the multi-layer targets and penetrating into the soil below multi-layer targets, the maximum value of penetration depths is 10.6D. Due to the low density and plasticity, penetration performance of EFP with aluminium liner is poor. EFP with aluminium liner are not through the upper layer of multi-layer targets. When the charge diameters are 100mm and 120mm respectively, the corresponding maximum values of penetration depths are 1.6D and 2.6D. For different liner materials and constant charge diameters, penetration depths caused by EFP with copper liner, steel liner and aluminium liner decrease in sequence. It indicates that the EFP with copper liner is ideal for larger penetration depths.

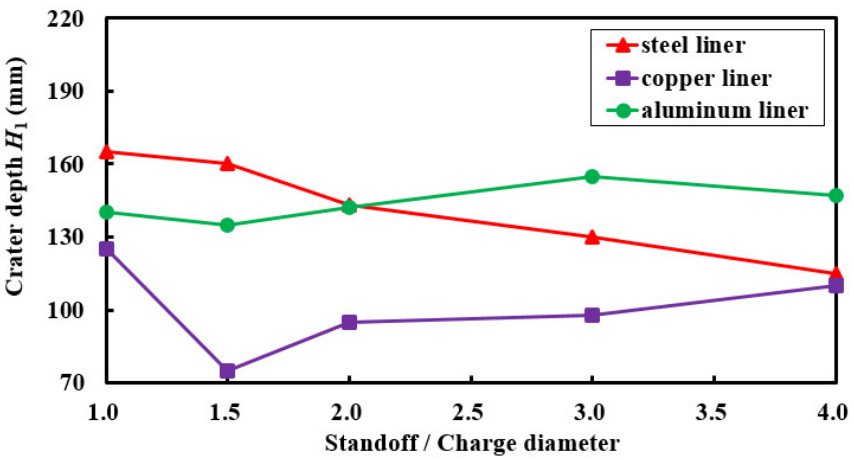

(a)

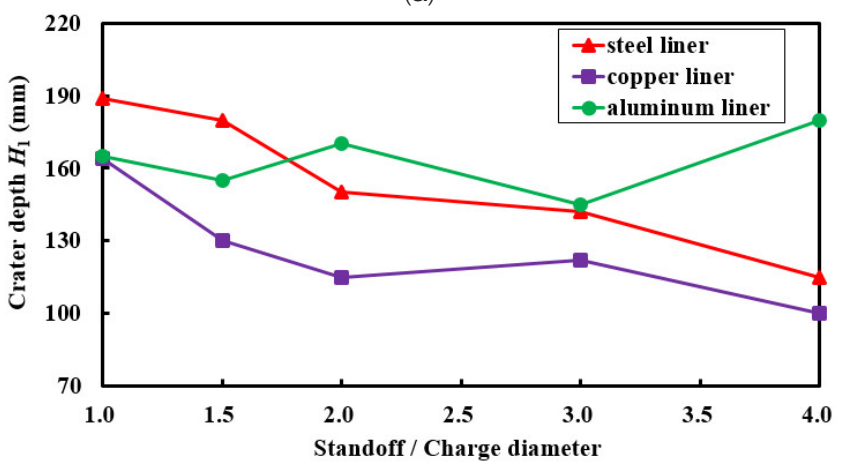

(b)

Figure 7: Variation trend of H_1 with different standoffs (a) D=100mm. (b) D=120mm

Table 4: Experimental results of penetration depth with different liner materials, charge diameters under different standoffs (mm)

Liner material	**Diameter (mm)**	**Standoff**				
		1D	**1.5D**	**2D**	**3D**	**4D**
Steel	100	315	340	385	470	560
	120	355	445	580	659	690
Copper	100	623	679	657	723	950
	120	629	700	1100	922	1270
Aluminum	100	140	135	142	155	150
	120	243	240	224	240	312

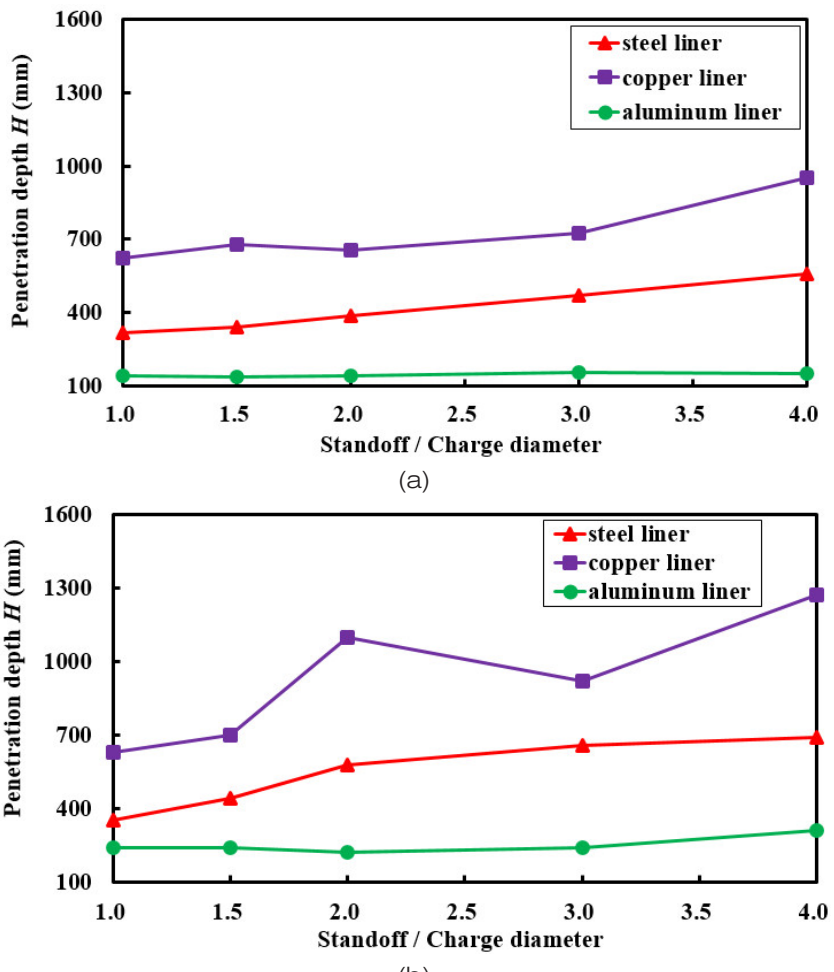

Figure 8: Variation trend of H with different standoffs (a) D=100mm. (b) D=120mm

4. NUMERICAL RESULTS

REMAP technology of the software AUTODYN is used to investigate the formation and penetration of EFP. The formation process of the EFP is simulated by Euler approach as shown in Figure 9. Then, the simulation results of EFP are imported and remapped into the Lagrange approach with local mesh refinement in the vicinity of the axis of the target as shown in Figure 10. The JWL, polynomial, porous and compaction equation of state are introduced to describe the Composition B, concrete, pebble and earth respectively. The transmit boundary condition is used between different target layers.

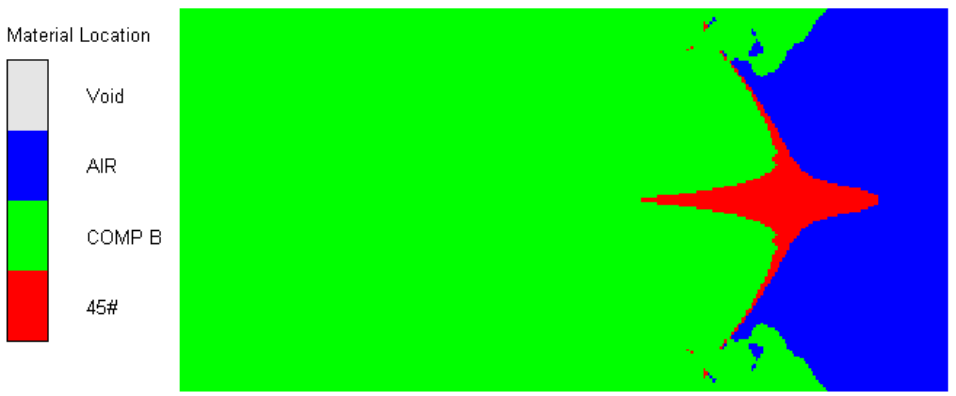

Figure 9: The typical simulation results of EFP formation

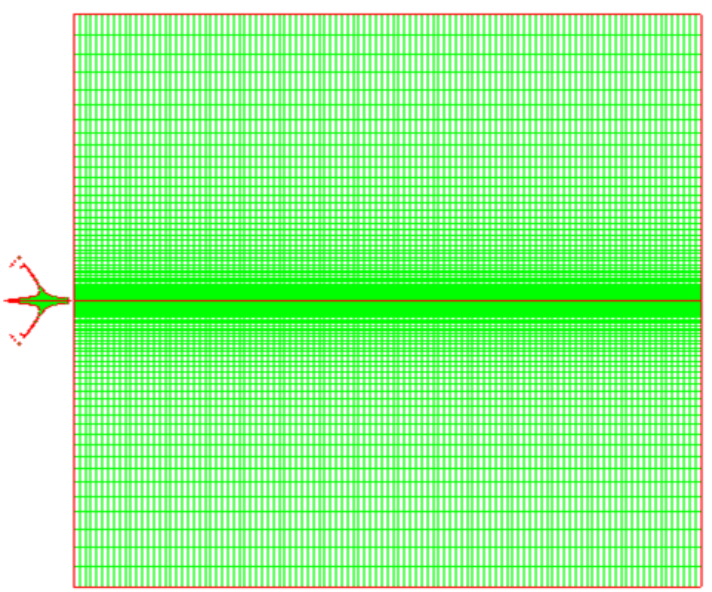

Figure 10: Simulation results of EFP remapped into Lagrange approach

Under the impact of the detonation wave, the liner moves inward and generates EFP. Figure 11 illustrates the EFP parameters, including the velocities, lengths and diameters of EFP in different standoffs. It is clear from Figure 11 that the EFP elongation with the increase of standoffs and the velocity gradient decrease with the length increase. In the case of 3D standoff, the fracture occurs in the neighbor of the EFP empennage.

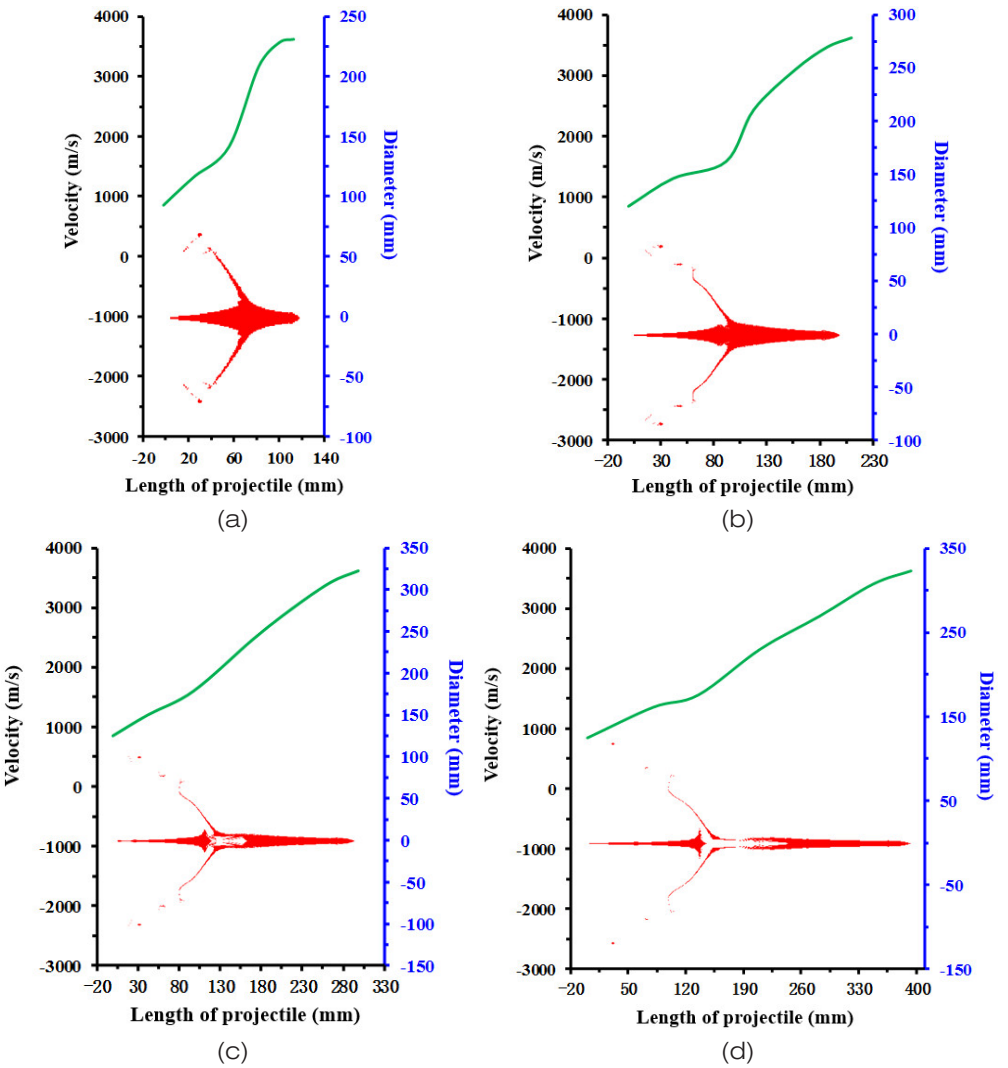

Figure 11: The EFP with steel liner and 120mm charge diameters under different standoffs; (a) 1D standoff. (b) 2D standoff. (c) 3D standoff. (d) 4D standoff

In the condition of 1D and 2D standoffs, the tip velocity of EFP with copper liner is similar to the velocity of EFP with steel liner. When the standoffs are 3D and 4D, for the same standoff, the tip velocity of EFP with copper liner is lower than steel liner. It is mainly caused by the velocity discontinuity of EFP with steel liner in the neighbor of the

empennage. Due to the high ductility of copper, in the 3D and 4D standoffs, The EFP with copper liner is continuous. However, The EFP with steel liner is fractured, as shown in Figures 11 and 12.

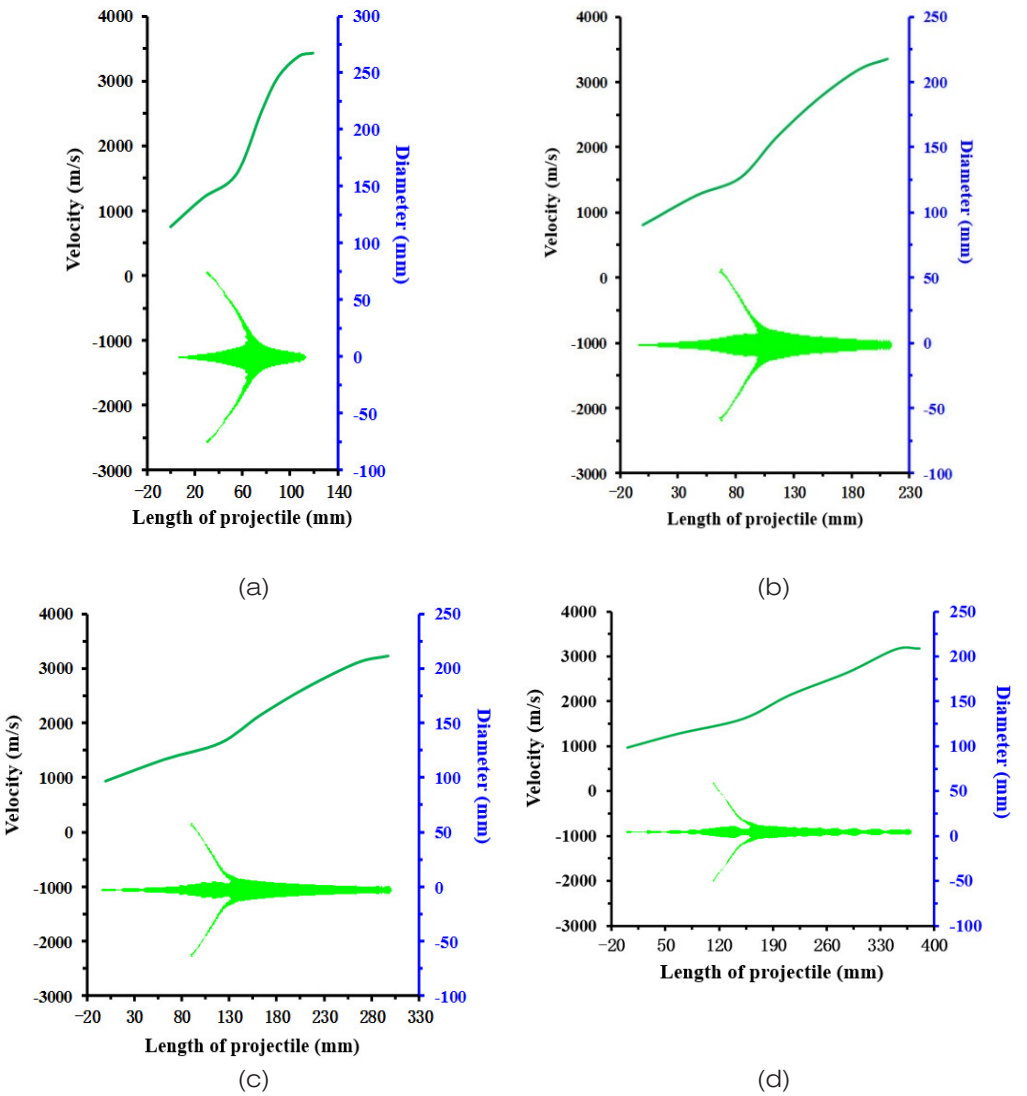

Figure 12: The EFP with copper liner and 120mm charge diameters under different standoffs; (a) 1D standoff. (b) 2D standoff. (c) 3D standoff. (d) 4D standof

Among different liner materials, for the same standoff, the tip velocity of EFP with aluminium liner is the highest, the length of EFP with aluminium liner is the shortest and the tail of EFP with aluminium liner is the smallest (Figures 11-13).

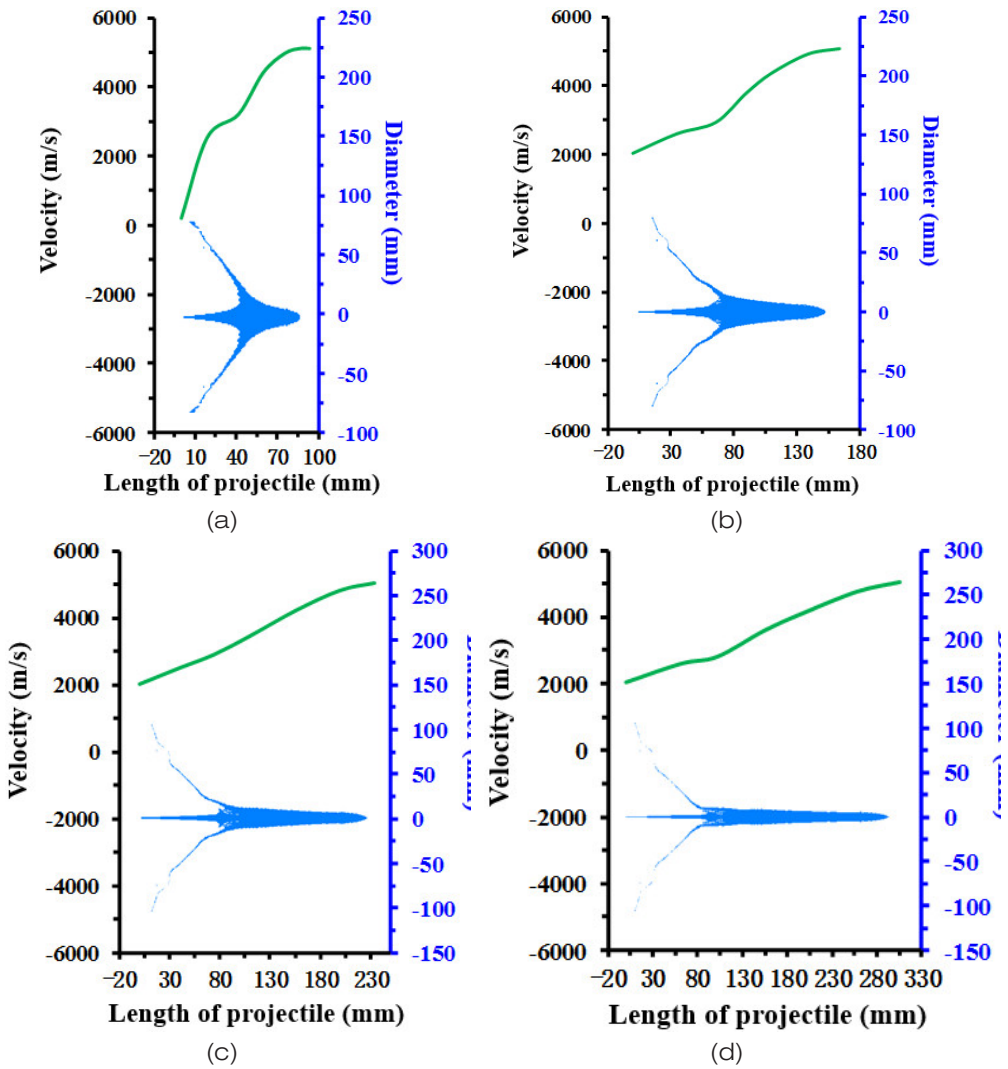

Figure 13: The EFP with aluminium liner and 120mm charge diameters under different standoffs; (a) 1D standoff. (b) 2D standoff. (c) 3D standoff. (d) 4D standoff

Table 5 shows the penetration depths by comparing numerical results with experimental ones. The maximum error of penetration depths caused by EFP is only 9.7%. It also demonstrates that the numerical techniques such as boundary conditions, mesh size, equations of state and so on are reasonable in this paper.

Compared with penetrating single concrete target, the interfacial effect exists obviously in the penetration of EFP into multi-layer targets, as shown in Figure 14. By the neighbor of the interface between concrete and pebble, the diameter of penetrating hole on the pebble side narrows locally, as shown in the location of P1. By the neighbor of the interface between pebble and rammed earth, the diameter of penetrating hole on the rammed earth

side enlarges locally, as shown in the location of P2. Under the influence of rarefaction wave, in the interface of pebble and rammed earth, the pebble generates ductile perforation and part of pebble invades rammed earth.

Table 5: Comparison between numerical and experimental results of penetration depth

Standoff	Liner material	Diameter (mm)	Experimental value (mm)	Numerical value (mm)	Error (%)
1D	Steel	100	315	343	8.9
		120	355	330	-7.0
	Copper	100	623	665	6.7
		120	629	676	7.5
	Aluminum	100	140	151	7.9
		120	243	261	7.4
1.5D	Steel	100	340	361	6.2
		120	445	487	9.4
	Copper	100	679	713	5.0
		120	700	765	9.3
	Aluminum	100	135	147	8.9
		120	240	259	7.9
2D	Steel	100	385	413	7.3
		120	580	530	-8.6
	Copper	100	657	680	3.5
		120	1100	1067	-3.0
	Aluminum	100	142	150	5.6
		120	224	245	9.4
3D	Steel	100	470	500	6.4
		120	659	645	-2.1
	Copper	100	723	735	1.7
		120	922	1011	9.7
	Aluminum	100	155	167	7.7
		120	240	261	8.8
4D	Steel	100	560	599	7.0
		120	690	650	-5.8
	Copper	100	950	700	-9.4
		120	1270	>1100	
	Aluminum	100	150	163	8.7
		120	312	335	7.4

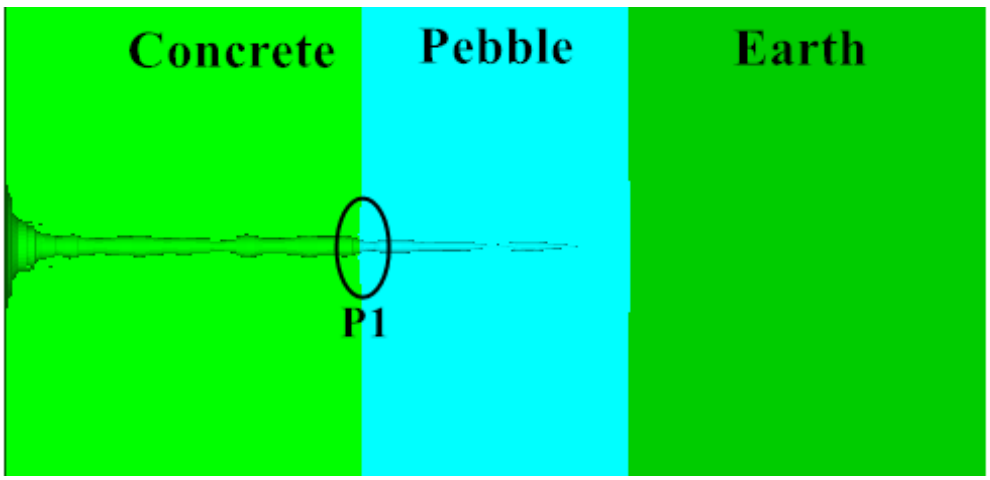

(a)

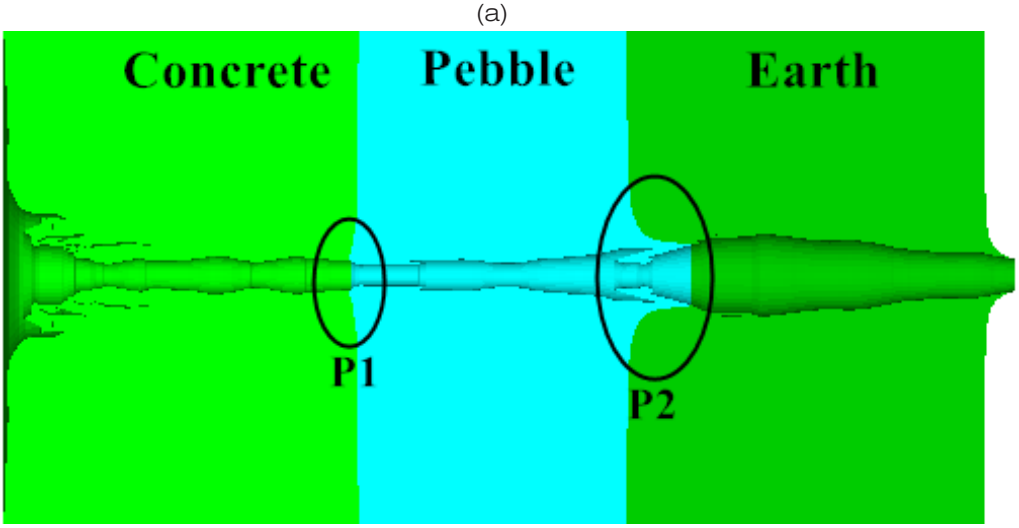

(b)

Figure 14: (a) Penetration results of EFP with steel liner materials and 120mm diameters in 4D standoff. (b) Penetration results of EFP with copper liner materials and 120mm diameters in 4D standoff

4. CONCLUSIONS

Following conclusious can be drawn from experimental and simulation analysis of EFP penetrating into multi-layer targets:

1. Crater diameters and depths formed by EFP with steel liner are the largest under condition of standoffs lower than 2D, however, when standoffs are greater than 2D, the crater diameters and depths formed by EFP with aluminium liner are the largest.
2. The optimal liner material of EFP to achieve a larger penetration hole diameters (D_2) and depth (H) are aluminium and copper, respectively.

3. Formation laws of crater diameter, hole diameter, crater depth and penetration depth with the variations in liner materials, charge diameters and standoffs are different. Therefore it is of great significance to take into comprehensive consideration all the impact factors to optimize the design of EFP.
4. All the experiments performed in this paper to investigate penetrating into multi-layer targets by EFP are also simulated numerically. The numerical results of penetration depth are in good agreement with the experimental ones.

ACKNOWLEDGEMENTS

This research is supported by the National Natural Science Foundation of China under grants 11325209 and 11521062.

REFERENCES

[1] Wen, H. M. and Y. Yang, A note on the deep penetration of projectiles into concrete. International Journal of Impact Engineering, 2014, 66: 1-4.

[2] Drathi, R., Das, A. J. M. and A. Rangarajan, Meshfree simulation of concrete structures and impact loading. International Journal of Impact Engineering, 2016, 91: 194-199.

[3] Wu, H., et al., Hard projectile perforation on the monolithic and segmented RC panels with a rear steel liner. International Journal of Impact Engineering, 2015, 76: 232-250.

[4] Nia, A. A., et al., Analysis of resistance of concrete target against penetration of eroding long rod projectile regarding flow field around the projectile tip. International Journal of Impact Engineering, 2013, 57: 36-42.

[5] Smith, J., et al., Discrete modeling of ultra-high-performance concrete with application to projectile penetration. International Journal of Impact Engineering, 2014, 65: 13-32.

[6] Guo, L., et al., Study mass loss at microscopic scale for a projectile penetration into concrete. International Journal of Impact Engineering, 2014, 72: 17-25.

[7] Warren, T. L., Forrestal, M. J. and P. W. Randles, Evaluation of large amplitude deceleration data from projectile penetration into concrete targets. Experimental Mechanics, 2014, 54(2): 241-253.

[8] Sherburn, J. A., et al., Meshfree modeling of concrete slab perforation using a reproducing kernel particle impact and penetration formulation. International Journal of Impact Engineering, 2015, 86: 96-110.

[9] Wang, C., Wang, W. J. and J. G. Ning, Investigation on shaped charge penetrating into concrete targets. Chinese Journal of Theoretical and Applied Mechanics, 2015, 47(4):672-686.

[10] Bian, H., et al., Numerical study of a concrete target under the penetration of rigid projectile using an elastoplastic damage model. Engineering Structures, 2016, 111: 525-537.

[11] Feng, J., et al., An armour-piercing projectile penetration in a double-layered target of ultra-high-performance fiber reinforced concrete and armour steel: Experimental and numerical analyses. Materials and Design, 2016, 102: 131-141.

[12] Yu, R., Spiesz, P., and H. J. H. Brouwers, Energy absorption capacity of a sustainable Ultra-High Performance Fibre Reinforced Concrete (UHPFRC) in quasi-static mode and under high velocity projectile impact. Cement and Concrete Composites, 2016, 68: 109-122.

[13] Zeng, B. Q., et al., 3D numerical simulation of oblique penetration of antirunway penetrator to multilayer runway target. ACTA ARMAMENTARII, 2007 28(12): 1433-1437.

[14] Xiao, J. G., et al., Demolition Mechanism and Behavior of Shaped Charge with Reactive Liner. Propellants, Explosives, Pyrotechnics, 2016.